scientific reports

Check for updates

OPEN

Designing cellulose based biochars for CO_2 separation using molecular simulations

Behnoush Barzegar & Farzaneh Feyzi✉

This study investigates the pyrolysis mechanism of cellulose using reactive molecular dynamics simulations to prepare biochars for CO_2 separation applications. Six biochars with densities ranging from 0.160 to 0.987 g/cm³ were prepared, and their performance in adsorbing CO_2, CH_4, and N_2 gases, as well as CO_2/CH_4 and CO_2/N_2 gas mixtures, was evaluated using Grand Canonical Monte Carlo (GCMC) simulations. The adsorption isotherms were fitted to the Dual-Site Langmuir (DSL) equation, and subsequently, the isosteric heat of adsorption, Gibbs free energy, and entropy changes were calculated. It was found that the results indicated that the density of biochar had a strong impact on gabs adsorption. CO_2 had much better interactions with biochars than CH_4 and N_2. The 0.351 g/cm³-density biochar presented the highest selectivity for CO_2. The effect of water vapor was also covered which remarkably decreased the adsorption of CO_2 by the competition of active sites for adsorption. These results indicate that optimized cellulose-derived biochars could be a promising material for CO_2 separation in sustainable gas purification technologies.

Keywords CO_2 capture, Cellulose pyrolysis, Biochar, Reactive force field molecular dynamics

The majority of global warming and climate change is caused by two greenhouse gases: methane (CH_4) and carbon dioxide (CO_2). Natural gas, consisting of methane, other light hydrocarbons and CO_2 is considered as one of the most appealing clean fuels in recent decades. However, the presence of CO_2 reduces the energy value of natural gas due to its dilution effect and, therefore, needs to be removed for effective use[1,2]. So far, various methods have been used for CO_2 separation. Among different common methods adsorption by solid adsorbents and membranes have received much attention because of low energy consumption, environmental friendliness, separation at ambient temperature, and ease of access to the separated phases[3–6]. Various adsorbents, such as glassy polymers[7,8], metal-organic frameworks (MOF)[9], zeolites[10], and carbonaceous materials[11–13], have been designed and used for this purpose. Carbon compounds, notably biochars, have received a lot of interest in recent decades due to their carbon-rich structure, stability, insolubility, and high aromatization[14]. Biochars are produced from the pyrolysis of biomass such as wood chips, peanut shells, straw and wood waste, industrial organic waste and urban sludge in an oxygen-free environment[15–20]. Biochar may be considered as an excellent CO_2 adsorber and a promising alternative to conventional solid carbon-based catalysts that are less environmentally friendly and economically inefficient[21].

High specific surface area and microporosity of biochars provide more active sites for CO_2 adsorption. Huang et al.[22] investigated and compared rice straw biochar produced using microwave and conventional pyrolysis. They found CO_2 adsorption amount of 80 mg/g at a temperature of 20 °C produced by microwave, which was 14% more than the biochars produced by conventional pyrolysis. This difference in the amount of CO_2 adsorption was due to the difference in specific surface area. The Mukherjee et al.[23] created biochar by pyrolyzing coffee grounds at three different temperatures (400, 500, and 600 °C), and studied CO_2 adsorption at 30 °C. The Brunauer-Emmett-Teller (BET) surface areas of biochars were 179, 311, and 539 m^2/g, respectively. According to their results, the highest amount of CO_2 adsorption was 2.8 mmol/g, which was achieved for the biochar made at 600 °C with the highest BET surface area. Serafin et al.[24] produced biochars using different biomasses. They showed that the precursor played a significant role on the structural properties of the resulting biochars. Only biochar with micropores in the 0.86 –0.3 nm range were efficient for CO_2 adsorption at 0 °C and 1 bar. The biochar from pomegranate peel with the micropores in the 0.3–0.57 nm range showed the highest quantity of 1.25 mmol/g CO_2 adsorption at 25 °C and 1 bar. Deng et al.[25], discovered that increasing the temperature from 0 to 75 °C reduced the range of micropores effective for CO_2 adsorption from 0.33 to 0.82 to 0.33–0.52 nm range. The best CO_2 adsorption capacity obtained at 25 °C and 1 bar, with the pore size in the range of 0.33–0.63 nm.

Thermodynamics Research Laboratory, School of Chemical Engineering, Iran University of Science and Technology, Tehran 16846-13114, Iran. ✉email: feyzi@iust.ac.ir

According to various studies, biochars are also highly effective for separating CO_2 from gas mixtures. Gonzalez et al.[26] studied the adsorption of CO_2 from a gas mixture (CO_2+N_2) containing 14 vol% CO_2 on the biochar made from almond shells. The selectivity of CO_2 was equal to 33 at 25 °C and 1 bar.

To determine the ability of biochars to separate CO_2, both experimental and theoretical studies have been conducted. The Ideal Adsorbed Solution Theory (IAST) has been widely applied with experimental data to estimate the selectivity of CO_2 adsorption from CO_2/N_2 mixtures[27], and valuable insights into the effectiveness of separation mechanisms have been inferred. By IAST method, the selectivity of CO_2 from gas mixtures containing 10–15 vol% CO_2+N_2 on biochars produced from pomegranate peel, wheat flour, and coconut shell were obtained as 15.1[24], 16.1[28], and 22[29], respectively, at 25 °C and 1 bar.

Generally, researches on biochars are more focused on synthesis methods and single-component CO_2 adsorption experimentally. Although IAST provides a method to investigate CO_2/N_2 binary adsorption, to the best of our knowledge, CO_2/N_2 and CO_2/CH_4 binary adsorption, effect of presence of water vapor, and thermodynamic properties have not been investigated. In this regard, molecular dynamics simulation (MD) can be a valuable tool for working on these cases. Cellulose is the main component of biomass structure which can be considered as an excellent adsorbent because of its high carbon yield, biodegradability, hydrophilicity, and low cost[30,31]. In addition, cellulose-based biochar does not suffer from pore blockage above the relative humidity threshold[32]. These properties make cellulose a promising material for producing biochars. So far, MD on cellulose pyrolysis is mainly focused on the materials formed at different temperatures and time intervals[33–35].

In this study, firstly cellulose-based biochars with different densities are produced by MD simulations. Then, Grand Canonical Monte Carlo (GCMC) simulations were performed to investigate the effect of density variations on gas adsorption. The adsorption of the pure gases CO_2, CH_4, and N_2, as well as the binary gas mixtures CO_2 (0.05)/CH_4 (0.95) and CO_2 (0.2)/N_2 (0.8), were studied. The effect of presence of water vapor on gas separation was also explored. For both pure and mixed-gas adsorption, the thermodynamic parameters including isosteric heat of adsorption, Henry's constant, Gibbs free energy change, and entropy change of adsorption, were determined. Dual-site Langmuir (DSL) adsorption model was also used to represent the isothermal data of pure and mixed-gas adsorption on biochars.

Methodology

Molecular model

The initial structure of cellulose was created with cellulose-builder software[36]. The fractional crystallographic coordinates used by this software were published by Nishiyama et al.[37]. The number of repeating D-glucose units in each chain was ten, making the degree of polymerization (DP) equal to 10. Twenty cellulose chains were created in a cubic cell with a side length of 81.39 Å using Packmol software[38]. The dimensions of the simulation box were chosen to avoid overlapping of atoms. Periodic boundary conditions were adopted to all directions.

Generation of biochar structure

The structures were subjected to annealing under the NVT ensemble (constant number of atoms, *N*; constant volume, *V*; and constant temperature, *T*) with a time-step of 1 fs for 0.2 ns from 300 to 700 K (higher than the glass transition temperature of cellulose $T_g \cong 500$ K). Then, the temperature was decreased to 300 K with a time-step of 1 fs for 0.2 ns. To create structures with different densities, the initial simulation box was placed under the NPT (constant number of atoms, *N*; constant pressure, *P*; constant temperature, *T*) ensemble at 1 bar and 300 K to the desired initial polymer densities (0.160, 0.351, 0.458, 0.648, 0.855, and 0.987 g/cm^3). The resulting systems were equilibrated for at least 200 ps at constant volume and temperature. This procedure allowed the chains to relax to stable configurations before applying the pyrolysis protocol. We used the Dreiding force field[39], that was used for cellulose repeatedly in previous simulation studies[40–45].

It is worth presenting a short description on ReaxFF's force field before explaining how the structures were built. The simulation based on the ReaxFF force field was performed to convert the cellulose to biochar and simulate the pyrolysis process. The bond order in ReaxFF is determined by the distance between atomic pairs and is updated at each time step. ReaxFF thus describes the formation and breakup of bonds in real-time. Van der Waals interactions in this force field are computed as distance-corrected Morse potentials and Coulomb interactions using EEM[46]. Reaction routes do not need to be predefined because ReaxFF can automatically handle changes related to chemical reactions based on atomic distance. This functionality is essential for the pyrolytic modeling of cellulose with many reactive sites[35]. ReaxFF defines the energy of the system as follows[47].

$$E_{\text{system}} = E_{\text{bond}} + E_{\text{over}} + E_{\text{under}} + E_{\text{val}} + E_{\text{pen}} + E_{\text{tors}} + E_{\text{conj}} + E_{\text{vdWaals}} + E_{\text{Coulomb}} \quad (1)$$

In Eq. (1) E_{system} and E_{bond} represent the system energy and the bond energy based on the corrected bond order, respectively. According to the valence theory of bonding, the overall bond orders of C and H should not exceed 4 and 1, respectively, which cannot be attained even after correcting the initial bond orders. E_{over} and E_{under} are therefore introduced to stand for over and under coordination, respectively. The valence angle is referred to as E_{val}. The penalty energy, known as E_{pen}, is used to reproduce the stability of systems in which two double bonds share one atom in a valence angle that is not taken into account by E_{val}. E_{tors} stands for the torsion angle energy, E_{conj} for the conjugation effect energy, E_{vdWals} for nonbonded van der Waals interactions, and $E_{Coulomb}$ for Coulomb interactions. Due to the Pauli's principle of orthogonalization and dispersion, these interactions and attraction energies are influential at short and long interatomic distances.

Reactive MD simulations were performed using NVT ensemble. We used the H/C/O ReaxFF parameters reported by Chenoweth et al.[48]. This force field has been applied many times to cellulose pyrolysis simulations successfully[33–35]. The Berendsen thermostat with a damping constant of 0.1 ps was adopted to control the system temperature. To balance the simulation accuracy and efficiency, a time step of 0.25 fs was considered. The MD

simulation for each structure started at the temperature of 300 K and continued to 1500 K with 100 K intervals. The result of each simulation was used as the initial structure for the simulation at the next temperature. Because of undesirable decomposition of smaller components, pyrolysis was not continued to temperatures above 1500 K. Biochars were then cooled down to 300 K step by step. The time of each simulation was set at 250 ps to prevent the conversion of components resulting from thermal decomposition into lighter materials such as CO_2 and H_2O. Figure 1 presents a schematic of this process. The simulations were performed with the Large-scale Atomic/Molecular Massively Parallel Simulator (LAMMPS)[49] version lammps-29Sep2021, with the USER-REAXC package. Furthermore, LAMMPS Python package was used to implement in situ detection of species based on bonding data extracted from LAMMPS during simulation runs.

Adsorption simulation

The adsorption of CO_2, CH_4, and N_2 gases on the six structures were investigated using GCMC simulation at 300 K and pressures ranging from 0.1 bar to 10 bar. Considering that no chemical reaction occurs during the adsorption, ReaxFF and Dreiding force field were implemented to describe the molecular and bonding interactions of biochars. CO_2 was modeled as a three-site, rigid linear molecule with a charged Lennard-Jones (LJ) interaction site on each atom. The LJ potential parameters for CO_2 were developed using Harris and Young's EPM2 force field[50]. The parameters for the all-atom CH_4 potential were taken from Liu et al.[51]. N_2 was considered as a three-site molecule, with two sites on the N atoms and a third on the center of mass[52]. Lorentz–Berthelot mixing rules were applied for calculating the interaction parameters between different atoms. In GCMC simulations, the adsorbent chemical potential (μ), V and T, are kept constant. GCMC cycles involved 10 exchanges (insertions and deletions) and 10 movements (translations and rotations).

First. the amounts of pure gases adsorption were examined. Then, the separation of binary gas mixtures CO_2 (0.05)/CH_4 (0.95) and CO_2 (0.2)/N_2 (0.8), with typical molar compositions of natural gas and flue gas, respectively, was investigated. These conditions are specifically chosen to evaluate the potential of the biochars in industrial applications of CO_2 separation, such as natural gas purification and post-combustion carbon capture. To account for the presence of water vapor, the partial pressure of H_2O in the mixtures was adjusted to its experimental saturation pressure (0.03537 bar, 300 K), while the ratios of CO_2/CH_4 and CO_2/N_2 were fixed at 0.05/0.95 and 0.2/0.8 in the bulk gas phase, respectively. The LJ potential parameters for H_2O were based on the SPC/E force field provided by Vega et al.[53]. The fugacity coefficients in the gas phase were ascertained using Peng-Robinson[54] equation of state. 5×10^6 configurations for the initial equilibrium were used followed by 2×10^7, 3×10^7, and 4×10^7 configurations for pure gases, binary gas mixtures, and gas mixtures + water vapor,

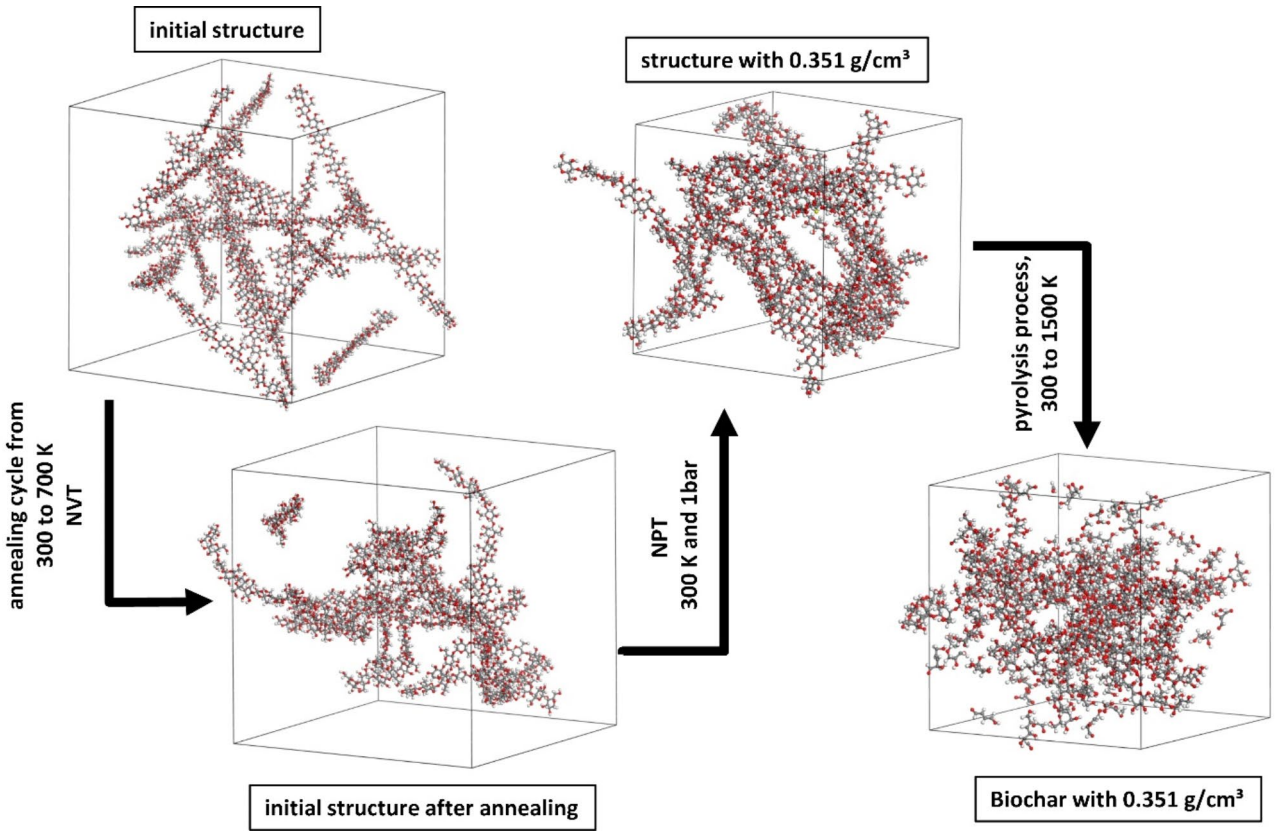

Fig. 1. Schematic of the process of creating biochar with density of 0.351 g/cm^3. Gray, white, and red spheres represent carbon, hydrogen, and oxygen atoms, respectively.

respectively. To further investigate the guest-host interactions Eq. 2 was used to calculate the isothermal heat of adsorption (Q_{st})[55].

$$Q_{st} = \frac{< NU > - < N >< U >}{< N^2 > - < N >< N >} + k_B T \quad (2)$$

where N is the total number of adsorbed gas molecules, U is the system potential energy, k_B is the Boltzmann constant, and angular brackets represent ensemble averages.

Results and discussions

Physical characterization

The products of pyrolysis

LAMMPS trajectories including the bond order were calculated using the Reax/c package[56]. Thermal decomposition of cellulose is illustrated in Fig. 2. According to the data obtained, pyrolysis began at 1300 K and continued to 1500 K, resulting in thermally decomposition of all the 20 cellulose molecules in the simulation box. Since pyrolysis began at 1300 K, only the results of 1300, 1400, and 1500 K are shown in Fig. 2.

A cumulative sum of some of the most common components produced from the pyrolysis process were calculated and are presented in Table S1 of Supplementary Information (SI). The biochar structure contains heavier components than shown in Table S1, but the most numerous ones are mentioned. As can be seen, $C_6H_mO_n$ and $C_2H_mO_n$ are the most significant components formed from pyrolysis. Their amounts increase as temperature increases, indicating cellulose molecules decompose into smaller pieces. The number of light molecules such as CHO_2, CH_2O, H_2O, and HO increase at higher temperatures.

Radial distribution function

The radial distribution function (RDF) was used to show the structure distribution of biochars as a function of distance. Figure 3a and b show the RDF diagrams of the biochars with different densities at a distance of 32 Å, and 4 Å, respectively. The RDF chart for biochar with a density of 0.160 g/cm^3 reaches a value of 1 around 30 Å, and, as the density increases RDF decreases. At the highest density (1.098 g/cm^3) RDF reaches unity around $r = 17$ Å. RDF fluctuations are insignificant at distances of $r > 10$ Å. For all the densities, RDF decreases as the density increases. Figure 3b shows that there is a significant peak at $r = 1.075$ Å which indicates the distance between carbon and hydrogen. The peak at $r = 0.975$ Å, represents the distance between oxygen and hydrogen. Next peak shows the distance between the closest oxygen atom and carbon at $r = 1.425$ Å. The final important peak at $r = 1.575$ Å shows the distance between two carbon atoms.

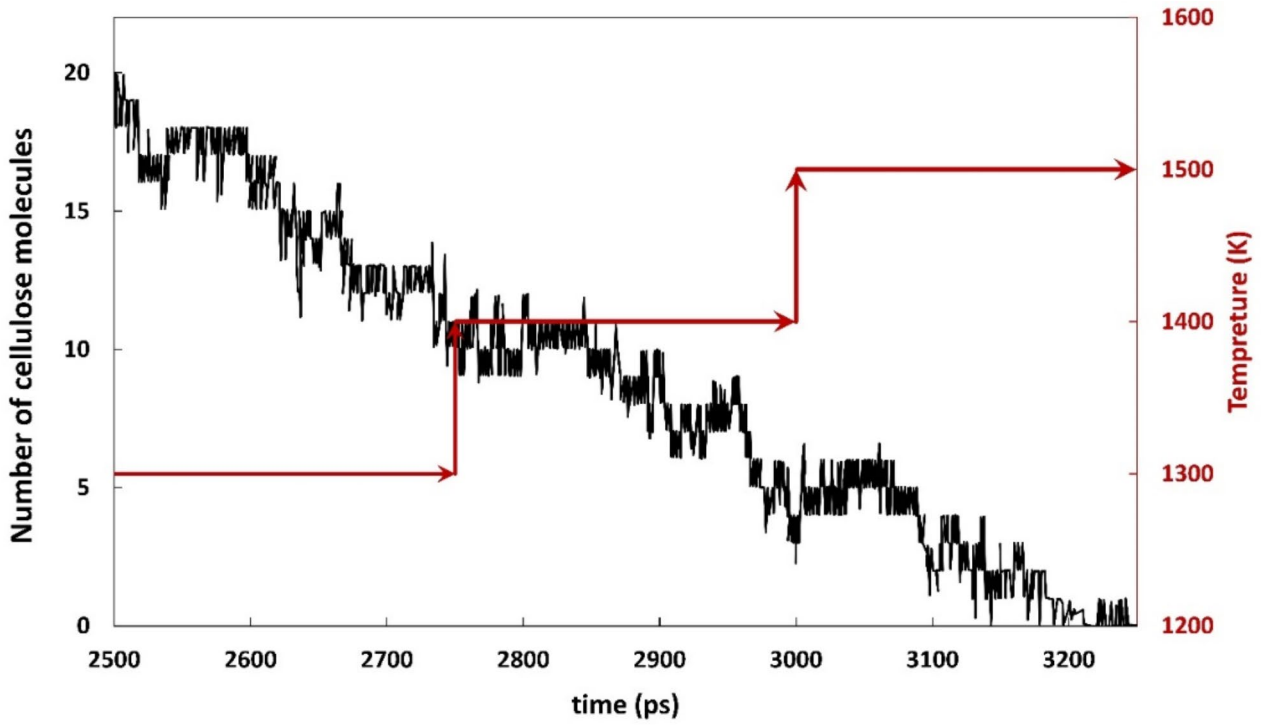

Fig. 2. Distribution of pyrolysis of cellulose obtained from ReaxFF MD simulations at 1300, 1400, and 1500 K.

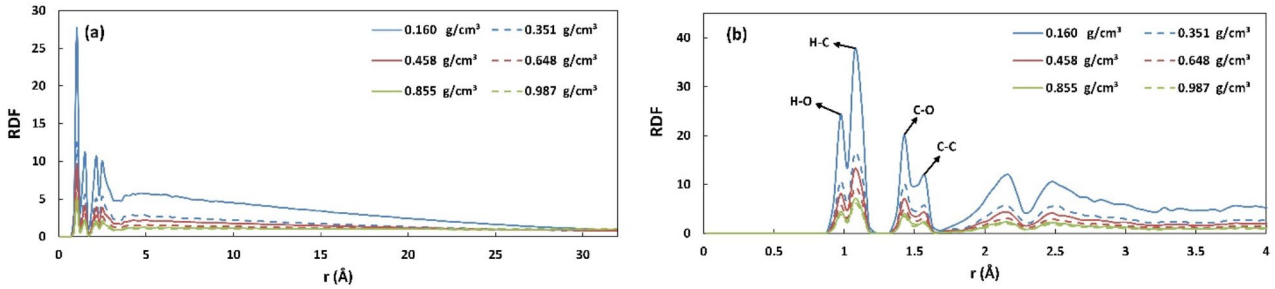

Fig. 3. RDF plot for all the simulated biochars (**a**) at a distance of 32 Å, and (**b**) at a distance of 4 Å.

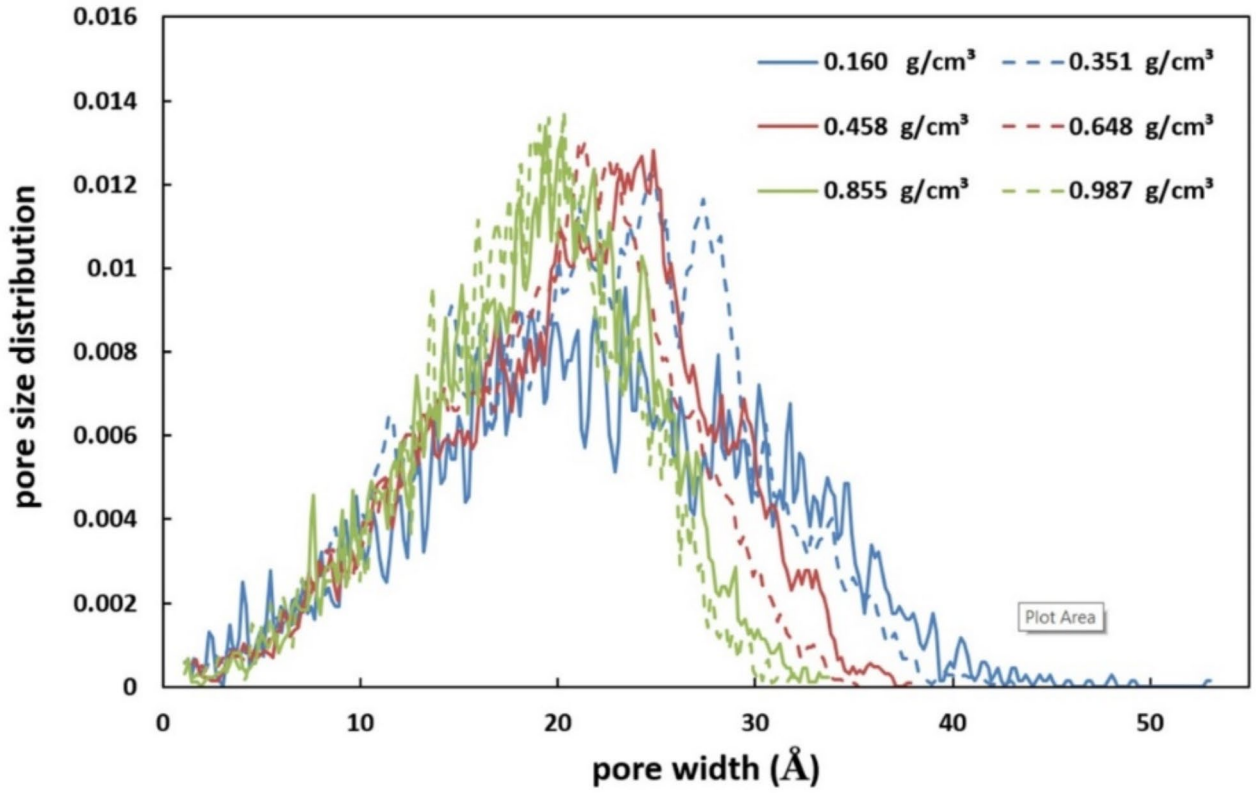

Fig. 4. Pore size distribution as a function of pore width for biochars with different densities.

Pore size distribution

Mass density is the main factor determining pore size. In many technological applications, biochars are useful because of their porosity as their most important property. A PoreBlazer v4.0 code[57,58] was used to calculate the pore size distribution (PSD) from geometric measurements taken from the simulation. PSDs of the biochars are shown in Fig. 4. As expected, the PSDs shift to smaller diameters as the density increases. The peaks appear at the pore widths of 25.84, 24.82, 24.02, 21.05, 20.16, and 18.51 Å for densities of 0.160, 0.351, 0.458, 0.648, 0.855, and 0.987 g/cm^3, respectively. It should be noted that an open structure allows for more space between biochar components, resulting in larger pores. Moreover, as the density increases, the PSDs become sharper and the variation in pore size decreases.

Pure gases adsorption on biochars

Using GCMC simulation amounts of pure CH_4, CO_2, and N_2 adsorption on biochars were obtained and compared. Figure 5 displays the adsorption isotherms at 300 K as a function of pressure. It is observed that the amount of adsorption of gases rise with pressure. CO_2 has a notable tendency to reach equilibrium at high pressures. All six biochars have a higher CO_2 adsorption amount, while N_2 has the lowest value. Quadrupole moment of CO_2 molecules is the main reason for higher interaction with the adsorbent surface. Considering CH_4 and N_2, it can be seen that by increasing the density of structures the amount of adsorption decreases, especially at higher pressures (3–10 bar). At densities higher than 0.648 g/cm^3, the rate of reduction of the

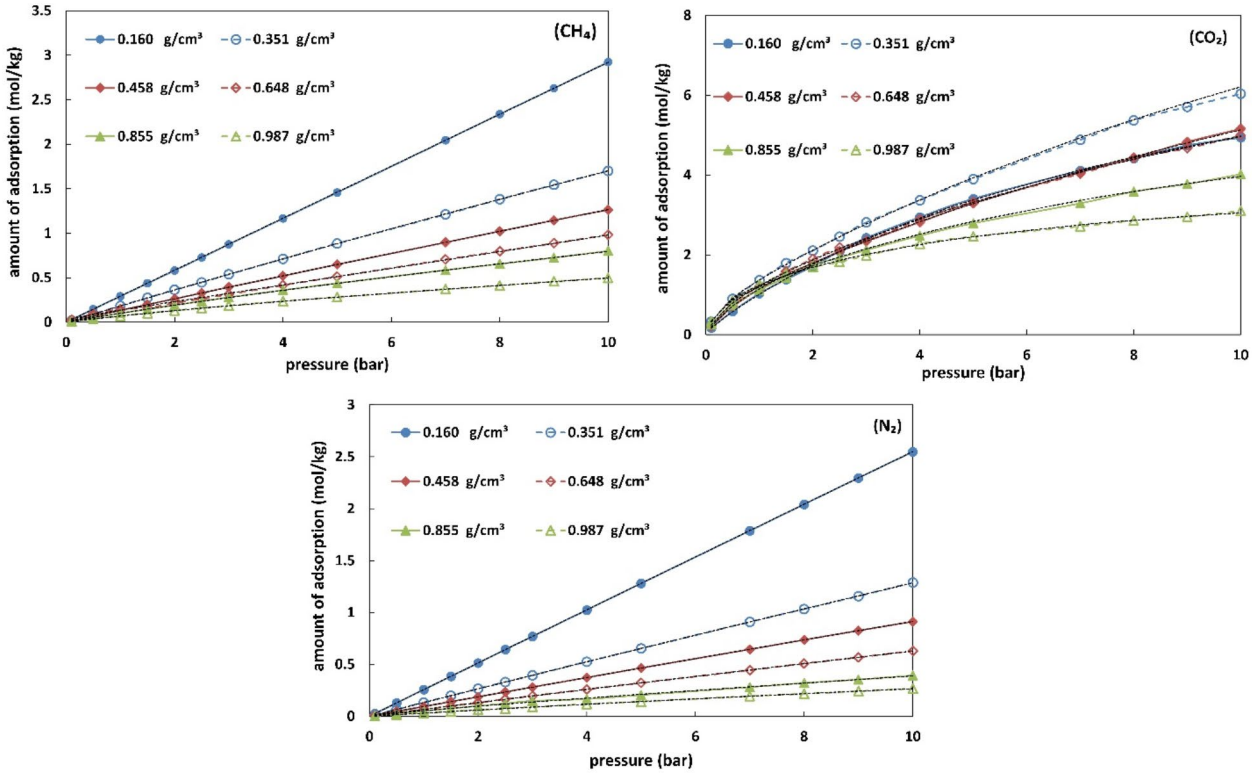

Fig. 5. Adsorption isotherms of pure CH_4, CO_2, and N_2 on six biochars with different densities as a function of pressure at 300 K. The circle, triangle, diamond, and square filled and unfilled with colorful lines and dashed lines represent the simulation results, and the black dashed lines illustrate DSL model.

amount of adsorption is slower. At a density of 0.987 g/cm^3, the amount of adsorption from 0.1 to 10 bar shows no remarkable change. CO_2 adsorption is slightly different from CH_4 and N_2. In general, it can be said that as the structure's density increases, the amount of CO_2 adsorption decreases. However, this trend is slightly different at lower densities. As can also be seen in Fig. 5, unlike CH_4 and N_2, where the highest adsorption amounts were related to the density of 0.160 g/cm^3, for CO_2 the highest amount was adsorbed on the structure with the density of 0.351 g/cm^3, followed by biochars with the densities of 0.458 and 0.648 g/cm^3.

The DSL model parameters were adjusted to pure gases isothermal adsorption data with very good accuracy. The results are presented in Table S2 of SI. Additionally, Section S.2 in SI contains the thermodynamic properties for pure gases, including isosteric heat of adsorption, Henry's constants, surface potential, Gibbs free energy, and entropy.

Mixed-gases adsorption on biochars

Figure 6 depicts the binary gas adsorption isotherms for the binary mixtures CO_2 (0.05)/CH_4 (0.95) and CO_2 (0.2)/N_2 (0.8) on biochars at 300 K and 0.1–10 bar. It is shown that the amount of CH_4 adsorption decreases with increasing biochar density. This result is consistent with the trend of pure CH_4 adsorption. At low pressures, all biochars adsorb CH_4 and CO_2 similarly. However, as the pressure increases the difference between adsorption amounts become more pronounced. As can also be seen from the CO_2 adsorption isotherms, the adsorption amount for the structure with the density of 0.351 g/cm^3 is higher than the other structures. Therefore, it is deduced that this adsorbent has a good ability for separating CO_2 even at 0.05 mol percent. Representation of the adsorption isotherms of binary mixture of CO_2 and N_2 is illustrated in Fig. 7. Similarly, for N_2, the amount of adsorption decreases with increasing biochar density. The amount of CO_2 adsorption is significantly higher than that of N_2, which indicates that the adsorbents have a high affinity for CO_2. The amount of CO_2 adsorption for the mixture of CO_2 and N_2 is also the highest at the density of 0.351 g/cm^3.

To investigate the separation performance, Eq. 3 was used to calculate the selectivity of separation[59].

$$S_{i,j} = (x_i/y_i)/(x_j/y_j) \tag{3}$$

where x and y are the mole fractions of components in the adsorbed phase and in the bulk phase, respectively, S is the selectivity and subscripts i and j represent the components. Figure 8 shows a comparison of adsorption selectivities of the biochars for both gas mixtures.

As shown for CO_2/CH_4 mixture, biochar with the density of 0.351 g/cm^3 at pressures of 0.1-4 bar has the highest selectivity for CO_2 separation. At pressures higher than 4 bar, biochar with the density of 0.648 g/cm^3

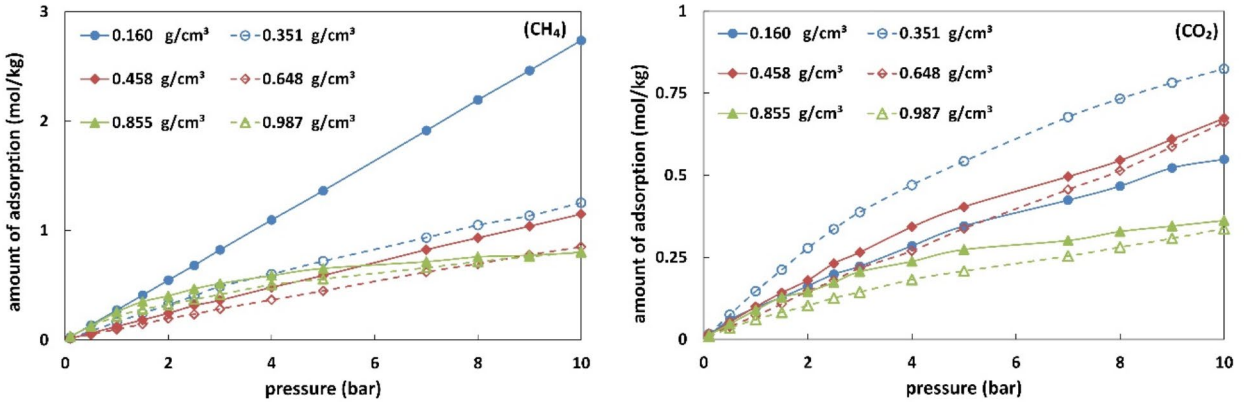

Fig. 6. Adsorption isotherms for CO_2 (0.05)/CH_4 (0.95) mixture on six biochars with different densities as a function of pressure at 300 K.

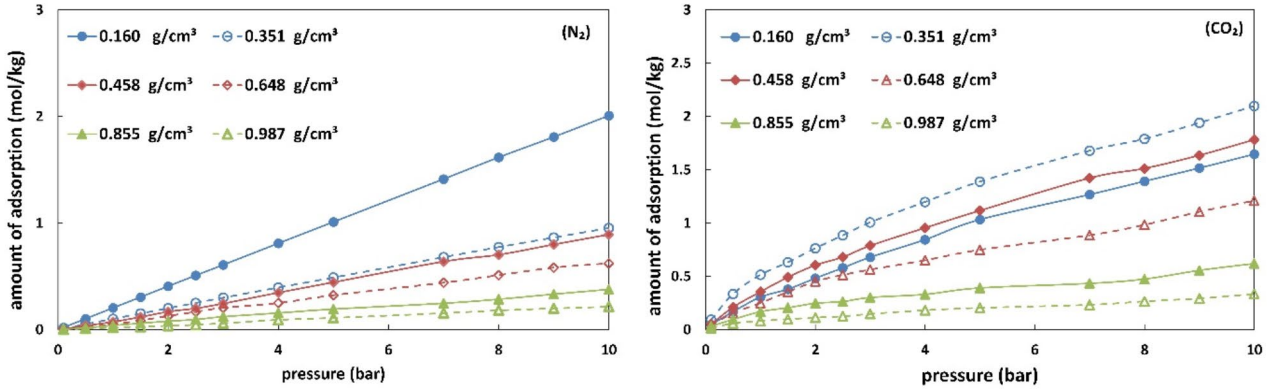

Fig. 7. Adsorption isotherms for CO_2 (0.2)/N_2 (0.8) mixture on six biochars with different densities as a function of pressure at 300 K.

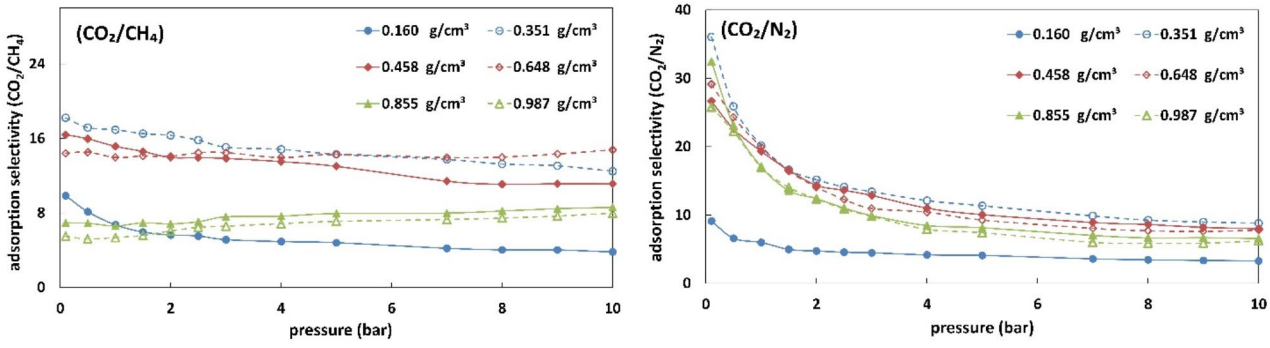

Fig. 8. Adsorption selectivity for (**a**) CO_2 (0.05)/CH_4 (0.95), (**B**) CO_2 (0.2)/N_2 (0.8) mixtures on six biochars with different densities as a function of pressure at 300 K.

shows the highest CO_2 selectivity. The reason can be explained by the fact that at pressures above 4 bar, the amount of CH_4 adsorption at the density of 0.648 g/cm^3 is lower than that at the density of 0.351 g/cm^3. As shown in Fig. 6, the amount of CO_2 adsorption at the density of 0.648 g/cm^3 shows the third-best performance. Graph of CO_2/N_2 mixture shows the biochar with the density of 0.351 g/cm^3 has the highest CO_2 selectivity among the other structures. It is also clear from comparing the two graphs that selectivity of the structures for CO_2/N_2 is far higher than CO_2/CH_4. Selectivities decline with increasing pressure and approach equilibrium at high pressures. The heterogeneity of the structures' surface energy can be the explanation for this tendency. Higher selectivity results from CO_2 preferentially occupying high-energy sites in the early stages of competitive adsorption.

With increasing pressure, molecules competitively occupy weaker positions; thus, selectivity decreases until equilibrium is achieved. In either case, it should be mentioned that the slope of the selectivity changes at low pressures is higher for the CO_2/N_2. This indicates that CO_2 is better adsorbed, and N_2 is less competitive than CH_4. For a more profound examination of the binary adsorption mechanism, the thermodynamic parameters of the two mixtures (CO_2/CH_4 and CO_2/N_2) are provided in Section S3 of SI.

Effect of the presence of water vapor on mixed-gas adsorption

Since biochar with the density of 0.351 g/cm^3 showed the highest CO_2 selectivity for both mixtures, it was chosen to explore the effect of presence of water vapor on adsorption. The molar ratios of the mixtures are introduced in "Adsorption simulation" Section. Figure 9 shows the results of the adsorption isotherms for the binary CO_2/CH_4 and CO_2/N_2 mixtures in the presence of water vapor. According to Fig. 9a, addition of water vapor to the gas mixture did not affect CH_4 adsorption significantly. However, CO_2 adsorption decreased due to competition between water vapor and CO_2. Amount of H_2O adsorption increases with pressure and is much higher than CO_2 and CH_4. This observation is the result of hydrogen bonding between the biochar's structure and water molecules. Cellulose conversion to biochar has created structures with hydrogen bonds, which have made them suitable substrates for H_2O adsorption. As it is illustrated in Fig. 9b, addition of water vapor to CO_2/N_2 gas mixture has a small effect on N_2 adsorption but strongly affects CO_2 adsorption. The contact surface of CO_2 molecules with the adsorbent surface has been decreased due to saturation of spaces by water molecules.

Conclusions

This work studied the influence of biochars with different densities, prepared from cellulose pyrolysis, on the adsorption of pure CO_2, CH_4, and N_2 gases, as well as mixed gases (CO_2/CH_4 and CO_2/N_2) using GCMC simulations. Results showed that higher biochar densities resulted in lower CH_4 and N_2 adsorption amounts. The adsorption amount of CO_2 was more on biochars with 0.351 and 0.458 g/cm^3 densities. Thermodynamic parameters were used to analyze the adsorption behavior. It was shown that CO_2 because of its quadrupole moment, had a more vital interaction with biochars than CH_4 and N_2, resulting in higher selectivity.

This study also examined the effect of water vapor on mixed-gas adsorption. Water vapor had little effect on CH_4 and N_2 adsorption, while it significantly inhibited CO_2 adsorption resulting from competition of hydrogen bonding with biochars' active sites. These results demonstrated that cellulose-derived biochars, particularly with certain specific densities, hold up as a good prospect for selective CO_2 separation and thus are likely to provide a sustainable and effective adsorbent for gas purification and greenhouse gas reduction technologies. Future research should focus on optimizing the properties of biochars and assessing their performances in large-scale gas separation processes. Moreover, deeper insight into the competition between CO_2 and O_2 on the surfaces of biochars under conditions of flue gas will further help in improving their industrial adsorption capabilities.

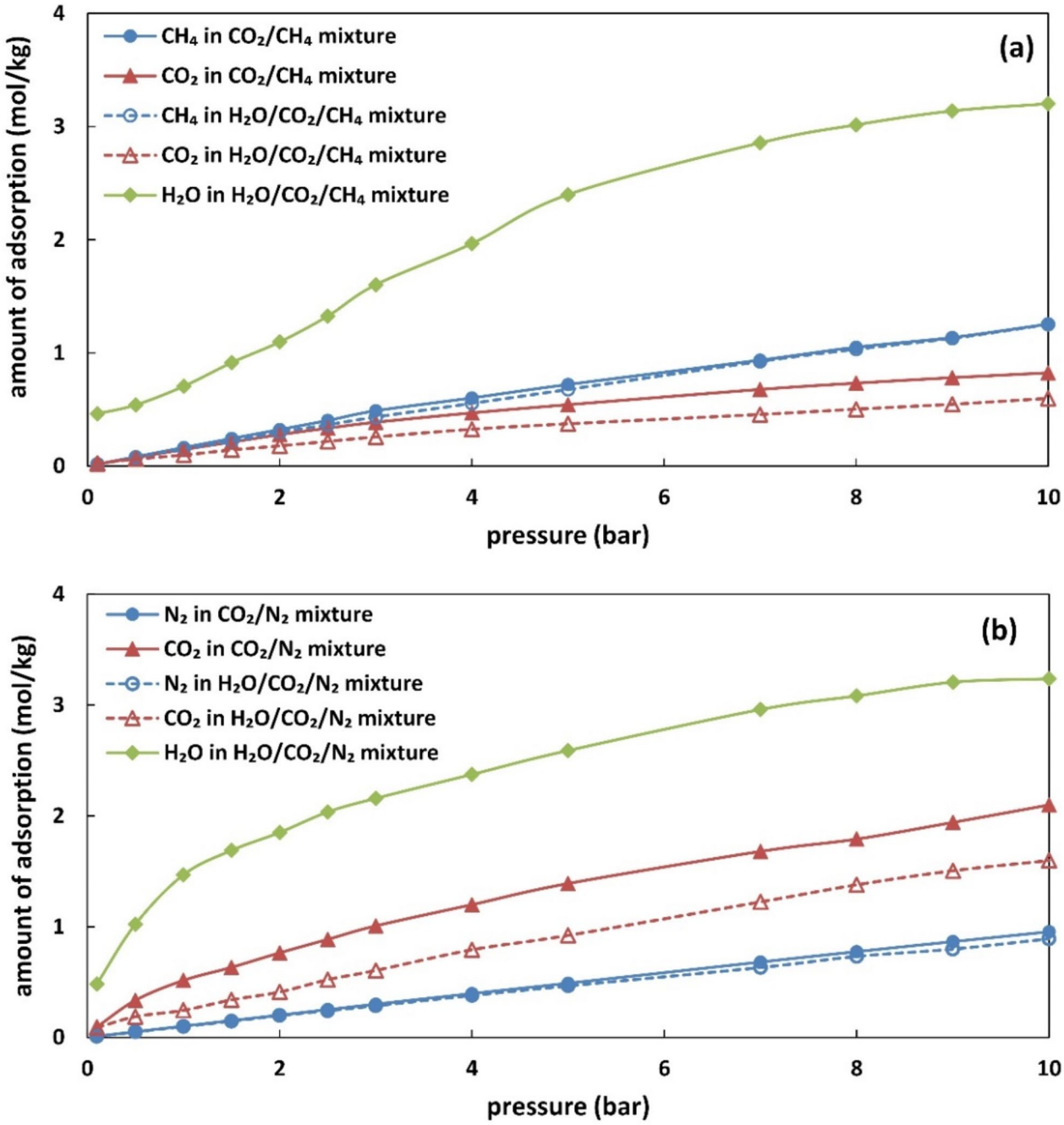

Fig. 9. Adsorption isotherms of (**a**) binary CO_2/CH_4 and ternary $H_2O/CO_2/CH_4$ mixtures and (**b**) binary CO_2/N_2 and ternary $H_2O/CO_2/N_2$ mixtures on the biochar with density of 0.351 g/cm^3 at 300 K as a function of pressure. The molar ratios of CO_2/CH_4 and CO_2/N_2 are 5/95 and 20/80 for both binary and ternary mixtures, respectively. The partial pressure of H_2O in both mixtures is 0.03537 bar.

Data availability

All data generated or analysed during this study are included in this published article (and its Supplementary Information files).

Received: 10 September 2024; Accepted: 9 January 2025
Published online: 10 January 2025

References

1. Carapellucci, R. & Milazzo, A. Membrane systems for CO_2 capture and their integration with gas turbine plants. *Proc. Inst. Mech. Eng. Part. J. Power Energy* **217**, 505–517 (2003).
2. Sharma, H. & Dhir, A. Capture of carbon dioxide using solid carbonaceous and non-carbonaceous adsorbents: A review. *Environ. Chem. Lett.* **19**, 851–873 (2021).
3. D'Alessandro, D. M., Smit, B. & Long, J. R. Carbon dioxide capture: Prospects for new materials. *Angew. Chem. Int. Ed.* **49**, 6058–6082 (2010).
4. Babarao, R., Jiang, J. & Sandler, S. I. Molecular simulations for adsorptive separation of CO_2/CH_4 mixture in metal-exposed, catenated, and charged metal-organic frameworks. *Langmuir* **25**, 5239–5247 (2009).
5. Shen, J. et al. Membranes with fast and selective gas-transport channels of laminar graphene oxide for efficient CO_2 capture. *Angew. Chem.* **127**, 588–592 (2015).
6. Bae, T. H. et al. Evaluation of cation-exchanged zeolite adsorbents for post-combustion carbon dioxide capture. *Energy Environ. Sci.* **6**, 128–138 (2013).
7. Kasahara, S., Kamio, E., Ishigami, T. & Matsuyama, H. Amino acid ionic liquid-based facilitated transport membranes for CO_2 separation. *Chem. Commun.* **48**, 6903–6905 (2012).
8. Shimoyama, Y., Komuro, S. & Jindaratsamee, P. Permeability of CO_2 through ionic liquid membranes with water vapour at feed and permeate streams. *J. Chem. Thermodyn.* **69**, 179–185 (2014).
9. Xue, W. et al. Effects of ionic liquid dispersion in metal-organic frameworks and covalent organic frameworks on CO_2 capture: A computational study. *Chem. Eng. Sci.* **140**, 1–9 (2016).
10. Siriwardane, R. V., Shen, M. S., Fisher, E. P. & Losch, J. Adsorption of CO_2 on zeolites at moderate temperatures. *Energy Fuels* **19**, 1153–1159 (2005).
11. Barzegar, B. & Feyzi, F. Effect of ionic liquids in carbon nanotube bundles on CO_2, H_2S, and N_2 separation from CH4: A computational study. *J. Chem. Phys.* **154**, 194504 (2021).
12. Rahmani, F., Nouranian, S. & Chiew, Y. C. 3D graphene as an unconventional support material for ionic liquid membranes: Computational insights into gas separations. *Ind. Eng. Chem. Res.* **59**, 2203–2210 (2020).
13. Barzegar, B. & Feyzi, F. Investigation of the effect of pristine and functionalized carbon nanotubes in cellulose acetate butyrate for mixed-gas separation: A molecular simulation study. *J. Mol. Liq.* **368**, 120788 (2022).
14. Lee, Y., Kim, Y. T., Kwon, E. E. & Lee, J. Biochar as a catalytic material for the production of 1,4-butanediol and tetrahydrofuran from furan. *Environ. Res.* **184**, 109325 (2020).
15. Rehman, K. et al. Cellulose decomposition and larval biomass production from the co-digestion of dairy manure and chicken manure by mini-livestock (Hermetia illucens L). *J. Environ. Manage.* **196**, 458–465 (2017).
16. Martín Juárez, J. et al. Effect of pretreatments on biogas production from microalgae biomass grown in pig manure treatment plants. *Bioresour. Technol.* **257**, 30–38 (2018).
17. Alakoski, E., Jämsén, M., Agar, D., Tampio, E. & Wihersaari, M. From wood pellets to wood chips, risks of degradation and emissions from the storage of woody biomass—A short review. *Renew. Sustain. Energy Rev.* **54**, 376–383 (2016).
18. Romero Millán, L. M., Vargas, S., Nzihou, A. & F. E. & Catalytic effect of inorganic elements on steam gasification biochar properties from agrowastes. *Energy Fuels* **33**, 8666–8675 (2019).
19. Li, J. et al. Investigation into lanthanum-coated biochar obtained from urban dewatered sewage sludge for enhanced phosphate adsorption. *Sci. Total Environ.* **714**, 136839 (2020).
20. Guo, S. et al. Recent advances in biochar-based adsorbents for CO_2 capture. *Carbon Capture Sci. Technol.* **4**, 100059 (2022).
21. Lee, J., Kim, K. H. & Kwon, E. E. Biochar as a catalyst. *Renew. Sustain. Energy Rev.* **77**, 70–79 (2017).
22. Huang, Y. F. et al. Microwave pyrolysis of rice straw to produce biochar as an adsorbent for CO_2 capture. *Energy* **84**, 75–82 (2015).
23. Mukherjee, A., Borugadda, V. B., Dynes, J. J., Niu, C. & Dalai, A. K. Carbon dioxide capture from flue gas in biochar produced from spent coffee grounds: Effect of surface chemistry and porous structure. *J. Environ. Chem. Eng.* **9**, 106049 (2021).
24. Serafin, J., Narkiewicz, U., Morawski, A. W., Wróbel, R. J. & Michalkiewicz, B. Highly microporous activated carbons from biomass for CO_2 capture and effective micropores at different conditions. *J. CO2 Util.* **18**, 73–79 (2017).
25. Deng, S. et al. Superior CO_2 adsorption on pine nut shell-derived activated carbons and the effective micropores at different temperatures. *Chem. Eng. J.* **253**, 46–54 (2014).
26. González, A. S., Plaza, M. G., Rubiera, F. & Pevida, C. Sustainable biomass-based carbon adsorbents for post-combustion CO_2 capture. *Chem. Eng. J.* **230**, 456–465 (2013).
27. Myers, A. L. & Prausnitz, J. M. Thermodynamics of mixed-gas adsorption. *AIChE J.* **11**, 121–127 (1965).
28. Hong, S. M., Jang, E., Dysart, A. D., Pol, V. G. & Lee, K. B. CO_2 capture in the sustainable wheat-derived activated microporous carbon compartments. *Sci. Rep.* **6**, 34590 (2016).
29. Yang, J. et al. Efficient CO_2 capture by porous carbons derived from coconut shell. *Energy Fuels* **31**, 4287–4293 (2017).
30. Rodrigues, S. C., Andrade, M., Moffat, J., Magalhães, F. D. & Mendes, A. Preparation of carbon molecular sieve membranes from an optimized ionic liquid-regenerated cellulose precursor. *J. Memb. Sci.* **572**, 390–400 (2019).
31. Ma, B., Qin, A., Li, X. & He, C. Preparation of cellulose hollow fiber membrane from bamboo pulp/1-butyl-3-methylimidazolium chloride/dimethylsulfoxide system. *Ind. Eng. Chem. Res.* **52**, 9417–9421 (2013).
32. Rodrigues, S. C., Andrade, M., Moffat, J., Magalhães, F. D. & Mendes, A. Carbon membranes with extremely high separation factors and stability. *Energy Technol.* **7**, 1801089 (2019).
33. Paajanen, A., Rinta-Paavola, A. & Vaari, J. High-temperature decomposition of amorphous and crystalline cellulose: Reactive molecular simulations. *Cellulose* **28**, 8987–9005 (2021).
34. Zheng, M. et al. Initial reaction mechanisms of cellulose pyrolysis revealed by ReaxFF molecular dynamics. *Fuel* **177**, 130–141 (2016).
35. Liu, Z., Ku, X., Jin, H. & Yang, S. Research on the microscopic reaction mechanism of cellulose pyrolysis using the molecular dynamics simulation. *J. Anal. Appl. Pyrol.* **159**, 105333 (2021).
36. Gomes, T. C. F. & Skaf, M. S. Cellulose-Builder: A toolkit for building crystalline structures of cellulose. *J. Comput. Chem.* **33**, 1338–1346 (2012).
37. Nishiyama, Y., Sugiyama, J., Chanzy, H. & Langan, P. Crystal structure and hydrogen bonding system in cellulose I α from synchrotron x-ray and neutron fiber diffraction. *J. Am. Chem. Soc.* **125**, 14300–14306 (2003).
38. Martínez, L., Andrade, R., Birgin, E. G. & Martínez, J. M. PACKMOL: A package for building initial configurations for molecular dynamics simulations. *J. Comput. Chem.* **30**, 2157–2164 (2009).
39. Mayo, S. L., Olafson, B. D. & Goddard, W. A. DREIDING: A generic force field for molecular simulations. *J. Phys. Chem.* **94**, 8897–8909 (1990).
40. Fernandes, S. Q. & Madhuranthakam, C. M. R. Molecular dynamics simulation of a superhydrophobic cellulose derivative targeted for eco-friendly packaging material. *Macromol. Theory Simul.* **30**, 2000056 (2021).
41. Mollahosseini, A. & Abdelrasoul, A. Zwitterionization of common hemodialysis membranes: assessment of different immobilized structure impact on hydrophilicity and biocompatibility of poly aryl ether sulfone (PAES) and cellulose triacetate (CTA) hemodialysis membranes. *Struct. Chem.* https://doi.org/10.1007/s11224-022-01940-0 (2022).
42. Krishna, S., Sreedhar, I. & Patel, C. M. Molecular dynamics study of thermal properties of polyamide nanocomposites reinforced with natural biofillers. *Mater. Today Chem.* **23**, 100756 (2022).

43. Anuar, N., Daid, W. M., Khalid, W. N. A. & Draman, S. A. S. Sheikh Abdullah, S. R. Prediction of interaction of citric acid modified cellulose with water region using molecular modelling technique. *Key Eng. Mater.* **797**, 118–126 (2019).
44. Chu, Y., Zhang, X., Hillestad, M. & He, X. Computational prediction of cellulose solubilities in ionic liquids based on COSMO-RS. *Fluid Phase Equilib.* **475**, 25–36 (2018).
45. Sáenz Ezquerro, C., Crespo Miñana, C., Izquierdo, S. & Laspalas, M. A molecular dynamics model to measure forces between cellulose fibril surfaces: On the effect of non-covalent polyelectrolyte adsorption. *Cellulose* **26**, 1449–1466 (2019).
46. Rappe, A. K. & Goddard, W. A. Charge equilibration for molecular dynamics simulations. *J. Phys. Chem.* **95**, 3358–3363 (1991).
47. van Duin, A. C. T., Dasgupta, S., Lorant, F. & Goddard, W. A. ReaxFF: A reactive force field for hydrocarbons. *J. Phys. Chem. A* **105**, 9396–9409 (2001).
48. Chenoweth, K., van Duin, A. C. T. & Goddard, W. A. ReaxFF reactive force field for molecular dynamics simulations of hydrocarbon oxidation. *J. Phys. Chem. A* **112**, 1040–1053 (2008).
49. Plimpton, S. Fast parallel algorithms for short-range molecular dynamics. *J. Comput. Phys.* **117**, 1–19 (1995).
50. Harris, J. G. & Yung, K. H. Carbon dioxide's liquid-vapor coexistence curve and critical properties as predicted by a simple molecular model. *J. Phys. Chem.* **99**, 12021–12024 (1995).
51. Liu, H., Dai, S. & Jiang, D. E. Solubility of gases in a common ionic liquid from molecular dynamics based free energy calculations. *J. Phys. Chem. B* **118**, 2719–2725 (2014).
52. Potoff, J. J. & Siepmann, J. I. Vapor-liquid equilibria of mixtures containing alkanes, carbon dioxide, and nitrogen. *AIChE J.* **47**, 1676–1682 (2001).
53. Vega, C., Sanz, E. & Abascal, J. L. F. The melting temperature of the most common models of water. *J. Chem. Phys.* **122**, 114507 (2005).
54. Peng, D. Y. & Robinson, D. B. A new two-constant equation of state. *Ind. Eng. Chem. Fundam.* **15**, 59–64 (1976).
55. Nicholson, D. N. G. P. *Computer Simulation and the Statistical Mechanics of Adsorption* (Academic Press Inc, 1982).
56. Aktulga, H. M., Fogarty, J. C., Pandit, S. A. & Grama, A. Y. Parallel reactive molecular dynamics: Numerical methods and algorithmic techniques. *Parallel Comput.* **38**, 245–259 (2012).
57. Sarkisov, L. & Harrison, A. Computational structure characterisation tools in application to ordered and disordered porous materials. *Mol. Simul.* **37**, 1248–1257 (2011).
58. Sarkisov, L. & Kim, J. Computational structure characterization tools for the era of material informatics. *Chem. Eng. Sci.* **121**, 322–330 (2015).
59. Fu, X. Y., Sotani, T. & Matsuyama, H. Effect of membrane preparation method on the outer surface roughness of cellulose acetate butyrate hollow fiber membrane. *Desalination* **233**, 10–18 (2008).

Author contributions

B.B. Conceptualization, Methodology, Validation, Formal analysis, Investigation, Writing the original draft, Visualization. F.F. Resources, Review and editing, Supervision, Project administration. All authors reviewed the manuscript.

Declarations

Competing interests

The authors declare no competing interests.

Additional information

Supplementary Information The online version contains supplementary material available at https://doi.org/10.1038/s41598-025-86254-x.

Correspondence and requests for materials should be addressed to F.F.

Reprints and permissions information is available at www.nature.com/reprints.

Publisher's note Springer Nature remains neutral with regard to jurisdictional claims in published maps and institutional affiliations.